



CHORUS

This is the accepted manuscript made available via CHORUS. The article has been published as:

Ultrafast x-ray and optical signatures of phase competition and separation underlying the photoinduced metallic phase in $\text{Pr}_{1-x}\text{Ca}_x\text{MnO}_3$

M. C. Langner, S. Zhou, G. Coslovich, Y.-D. Chuang, Y. Zhu, J. S. Robinson, W. F. Schlotter, J. J. Turner, M. P. Minitti, R. G. Moore, W. S. Lee, D. H. Lu, D. Doering, P. Denes, Y. Tomioka, Y. Tokura, R. A. Kaindl, and R. W. Schoenlein

Phys. Rev. B **92**, 155148 — Published 29 October 2015

DOI: [10.1103/PhysRevB.92.155148](https://doi.org/10.1103/PhysRevB.92.155148)

Ultrafast X-ray and Optical Signatures of Phase Competition and Separation Underlying the Photo-induced Metallic Phase in $\text{Pr}_{1-x}\text{Ca}_x\text{MnO}_3$

M.C. Langner,¹ S. Zhou,^{1,2} G. Coslovich,¹ Y.-D. Chuang,² Y. Zhu,¹ J.S. Robinson,¹ W.F. Schlotter,³ J.J. Turner,³ M.P. Minitti,³ R.G. Moore,⁴ W.S. Lee,⁴ D.H. Lu,⁵ D. Doering,⁶ P. Denes,⁶ Y. Tomioka,⁷ Y. Tokura,^{8,9} R.A. Kaindl,¹ and R. W. Schoenlein¹

¹Materials Science Division, Lawrence Berkeley National Laboratory, Berkeley, CA 94720, USA

²Advanced Light Source, Lawrence Berkeley National Laboratory, Berkeley CA 94720, USA

³Linac Coherent Light Source, SLAC National Accelerator Laboratory, Menlo Park, California 94720, USA

⁴Stanford Institute for Materials and Energy Science, SLAC National Accelerator Laboratory, Menlo Park, California 94720, USA

⁵Stanford Synchrotron Radiation Lightsource, SLAC National Accelerator Laboratory, Menlo Park, California 94720, USA

⁶Engineering Division, Lawrence Berkeley National Laboratory, Berkeley, California 94720, USA

⁷Nanoelectronics Research Institute, National Institute of Advanced Industrial Science and Technology (AIST) Tsukuba Central 4, 1-1- Higashi Tsukuba 305-8562, Japan

⁸Department of Applied Physics and Quantum Phase Electronics Center, University of Tokyo, Tokyo 113-8656, Japan

⁹RIKEN, Center for Emergent Matter Science, Wako 351-0198, Japan

(Dated: October 6, 2015)

The coexistence of ferromagnetic and antiferromagnetic phases, and their role in the photo-induced insulator-to-metal transition in $\text{Pr}_{1-x}\text{Ca}_x\text{MnO}_3$ are revealed via ultrafast resonant x-ray diffraction and broadband optical reflectivity measurements. The antiferromagnetic scattering signal and ferromagnetically sensitive reflectivity measurements show similar, strongly temperature dependent timescales. We attribute the common dynamics to an activation barrier between the equilibrium insulating phase and the photo-induced metallic phase related to interactions between the phase separated ferromagnetic and antiferromagnetic insulating phases.

PACS numbers: 64.60.-i, 75.47.Gk, 78.47.J-

INTRODUCTION

Rich phase diagrams in strongly-correlated electron systems result from interplay between energetically similar ground states with vastly different properties [1–3]. At the phase boundaries, a phase-separated ground state can form, consisting of a spatially inhomogeneous mixture of the pure ground states that exist on either side of the boundary [4]. This phase separation is thought to play a critical role in the colossal magneto-resistance effect in manganites, where the conductivity increases by several orders of magnitude through the application of a magnetic field [5].

$\text{Pr}_{1-x}\text{Ca}_x\text{MnO}_3$ (PCMO) is unique among the manganites, in that the equilibrium state is insulating regardless of temperature and doping. The colossal magneto-resistance (CMR) effect occurs in a doping region ($0.3 < x < 0.5$) that lies between a ferromagnetic (FM) phase at low doping ($x < 0.3$) fig 1(a) and an antiferromagnetic (AFM) phase at half doping. The CMR effect is commonly described as a transition mediated by the percolation of metallic clusters, however both of the pure FM and AFM phases in PCMO are robustly insulating, suggesting that the magnetic-field induced metallic state represents a distinct phase from the equilibrium FM and AFM phases.

At $x = 0.3$, the sample has a charge-ordering (CO) transition at $T_{CO} = 220$ K, an AFM transition at $T_N = 140$ K, and a transition to a mixed FM/AFM state at $T_{F/A} = 120$ K (figure 1(a,b)). The $x=0.5$ sample lacks the mixed FM/AFM state, and exhibits slightly higher temperatures for the CO and AFM transitions.

Optical excitation is also known to induce a meta-stable metallic phase in PCMO [6], and the nature of this phase,

particularly in regards to the magnetic ordering, has been the subject of considerable debate [6–10]. Moreover, the optically-induced metallic state in PCMO can be created either through the resonant excitation of a lattice mode or by photo-doping with near IR wavelengths[9–12], where the primary excitation is thought to occur on sites with Mn^{3+} valence [8, 13].

The magnetic field-induced metallic state differs significantly from the ground states at high or low doping, and the photo-induced metallic (PIM) state is again distinct from the field-induced metallic (FIM) state, representing a fourth, meta-stable state of the system; optical spectra show significant differences between the FIM and PIM states[14–17]. An applied electric field combined with an optical excitation can stabilize the PIM state indefinitely, but under optical excitation alone, the PIM state is relatively short-lived[6]. In contrast, at low temperature (below ~ 50 K) and with appropriate doping, the FIM state is persistent until the sample is heated [5].

The differences in behavior between the PIM and FIM states are related to the metallic magnetic phase through coupling of the magnetic alignment to the lattice strain and subsequent frozen-in grain boundaries [18–23]. The PIM and FIM perturb the magnetic state in different ways; spins are aligned by the applied magnetic field in the CMR effect but are disordered through photo-excitation.

Here we combine ultrafast x-ray and optical techniques to reveal that separation and interaction between ferromagnetic and antiferromagnetic phases underlies the transient metallic phase in PCMO. We observe that the pseudo-equilibrium metallic state is not achieved for several picoseconds in the

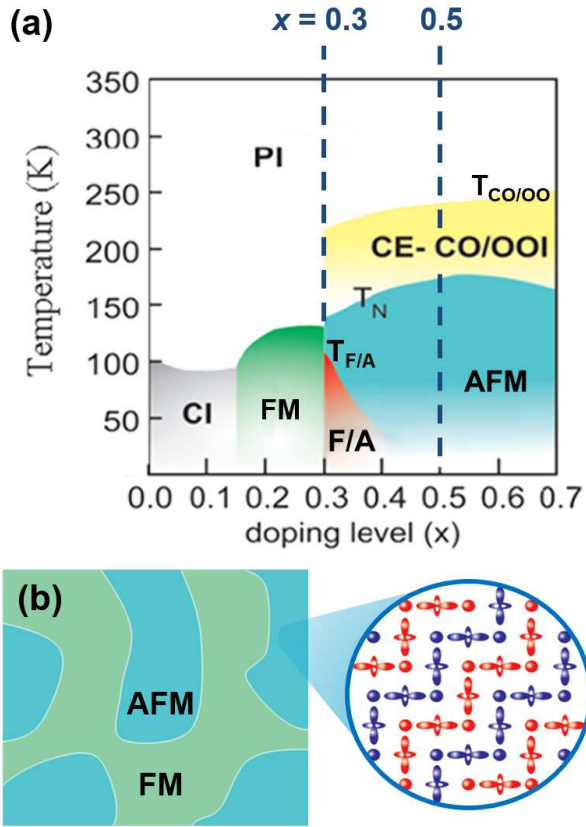


FIG. 1. (a) Phase diagram for $\text{Pr}_{1-x}\text{Ca}_x\text{MnO}_3$. (b) Diagram of mixed F/A phase showing real-space antiferromagnetic configuration.

mixed phase ($x=0.3$), while it promptly reached on sub-picosecond timescales in the pure AFM state ($x=0.5$). Our results suggest the presence of a strong coupling between competing phases, likely the result of lattice distortions, plays a key role in the insulator to metal transition.

EXPERIMENTAL

We utilize ultrafast resonant x-ray diffraction (RXD) and ultrafast broadband optical spectroscopy to provide important new insight into the nature of the photo-induced metallic phase in PCMO. RXD in PCMO at the critical doping of $x = 0.3$ was performed at the soft x-ray beamline at the Linac Coherent Light Source, utilizing an energy of 640 eV, resonant with the Mn L-edge, on the $(1/4, 1/4, 0)$ scattering peak, which is a direct measure of the antiferromagnetic order parameter [24, 25]. Ultrafast optical spectroscopy was performed in the mixed phase region ($x = 0.3$ doping) and in the pure AFM state ($x = 0.5$ doping). The measured spectra cover a range of energies from 1.3 eV to 2.8 eV, where the optical constants are sensitive to optical charge transfer and inter-site d-to-d transitions [26]. In all measurements, the sample was excited at an energy of 1.5 eV, which has been shown to

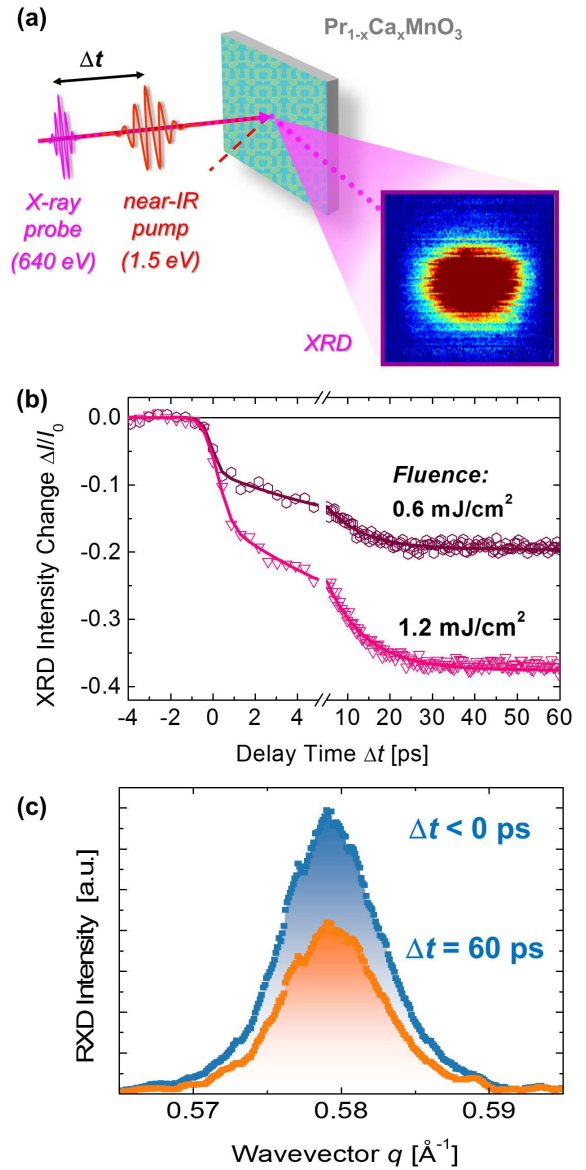


FIG. 2. (a) Diagram of experimental showing real-space antiferromagnetic configuration and measured diffraction peak image. (b) Dynamics of the scattering intensity of the $(1/4, 1/4, 0)$ AFM diffraction peak for 0.6 and 1.2 mJ/cm^2 (c) Scattering peak profiles for $t < 0$ (top curve) and $t = 60$ ps (bottom curve) with an excitation fluence of 1.2 mJ/cm^2 .

duce a metallic state. [7, 12].

We performed ultrafast RXD measurements at $x=0.3$ doping with the experimental geometry illustrated in figure 2(a). The scattering signal shows a clear reduction of intensity following optical excitation. We observed no significant changes to the scattering angle or peak width, indicating that above band-gap excitation does not change the ordering wavevector or correlation length, even while significantly suppressing the AFM order parameter. The time dependence of the scattering intensity at 60 K is shown in figure 2(b). The spin-ordering is reduced in two stages, a prompt reduction is observed on

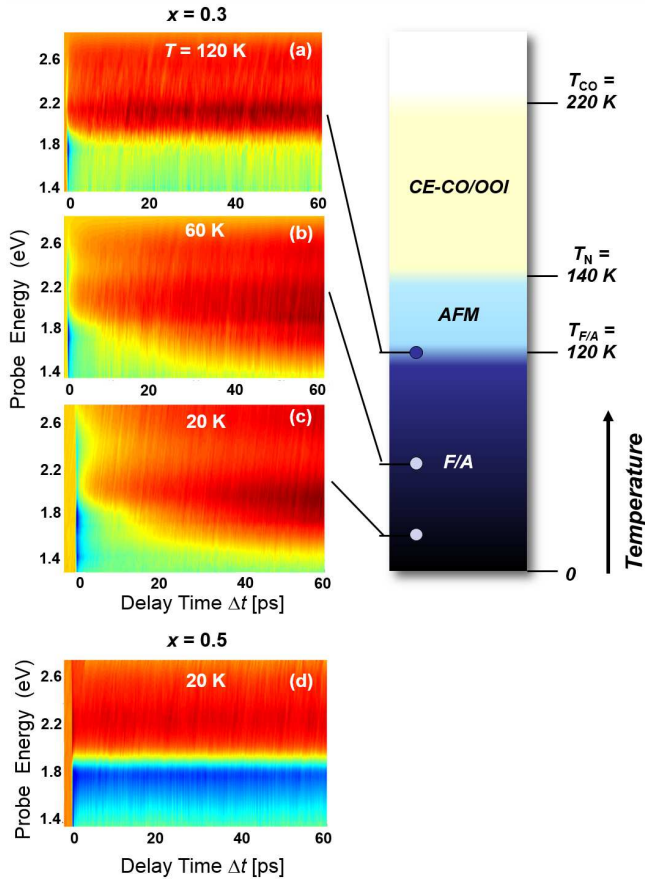


FIG. 3. Color maps of dR/R data as a function of pump/probe time-delay and probe wavelength. (a) $x = 0.3$, $T = 20$ K, (b) $x = 0.3$, $T = 60$ K, (c) $x = 0.3$, $T = 120$ K and (d) $x = 0.5$, $T = 20$ K. In the $x = 0.3$ sample, the low temperature spectral dynamics are clearly slower than in the $x = 0.5$ sample, but above 120 K the $x = 0.3$ spectra become similar to the $x = 0.5$ spectra.

a timescale of ~ 300 fs, corresponding to the time resolution of the x-ray probe, and a further loss of intensity develops on a time scale of ~ 9 ps. With increasing excitation fluence, spin ordering is further reduced, but the dynamics remain unchanged. Furthermore, the characteristic correlation length of the AFM diffraction peak remains unchanged throughout the excitation and recovery of the AFM order as indicated in figure 2(c). The invariance of the diffracted peak width, even when the intensity of the AFM signal is reduced significantly, suggests that the characteristic AFM domain size remains unchanged down to a length scale of 1400 \AA .

Important complementary insight can be obtained from the dynamics probed via the ultrafast broadband visible probe. For the $x=0.3$ doped mixed-phase sample, the intermediate 9 ps time-constant is also evident in the time-resolved optical reflectivity data, but notably the single AFM phase $x=0.5$ sample shows no dynamics on this time-scale. Time-resolved broadband optical data is shown in figure 3(a-d), for three temperatures at a doping of $x = 0.3$ and at low temperature for $x = 0.5$. The $x=0.5$ sample and the $x=0.3$ at 120 K show an edge

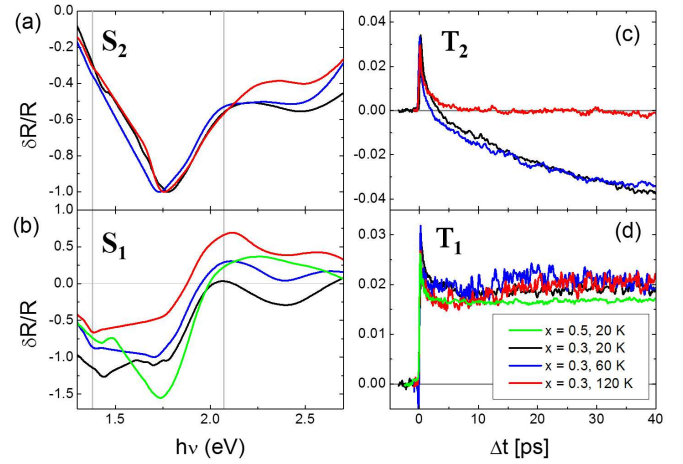


FIG. 4. Spectral components of the data in figure 3(a-d). The $x = 0.3$ sample shows two spectral components, shown in (a) and (b), while the $x = 0.5$ data can be described with only the component shown in figure (b). The two dimensional data in figure 3 can be reconstructed by multiplying the spectral component (figures (a) and (b)) with the temporal component (figures (c) and (d)), and summing these products, such that δR is described by equation 1.

in the spectrum at 1.7 eV, and the signal remains constant at timescales longer than 5 ps. At low temperature in the $x=0.3$ sample (20K, 60k), slower dynamics are apparent with an additional peak in the spectrum.

Similar to the RXD studies, optical spectroscopy exhibits dynamics over multiple time-scales. At a doping of $x = 0.3$, three time-scales are observed at low temperatures: a fast component with a time-constant of ~ 0.5 ps (τ_1), an intermediate component at 3-10 ps (τ_2), and a very slow component extending beyond the measured time-window ($\gg 60$ ps, τ_3). Optical data at a doping of $x = 0.5$ shows the fast (0.5 ps) and slow ($\gg 60$ ps) components but lacks the intermediate component observed in the $x=0.3$ sample. For both dopings, the onset of the dynamics is limited by the probe resolution of 100 fs, consistent with previous measurements [7, 9, 12].

A singular value decomposition of the broadband reflectivity data into spectral and temporal components is shown in figure 4 [27–29]. This decomposition describes the data as independent spectral and temporal functions, such that the overall reflectivity change $\delta R(\Delta t, h\nu)$ is described as:

$$\delta R(\Delta t, h\nu) = \sum_{i=1} S_i(h\nu) T_i(\Delta t). \quad (1)$$

The functions S_i and T_i represent the independent spectral and temporal components, respectively.

The $x=0.5$ data consists of a *single* spectral component (S_1 , green line), with dynamics characterized by time constants τ_1 and τ_3 , which we refer to as the fast component and slow remnant component.

The $x = 0.3$ data can be decomposed into two spectral components: (1) a step-like component (S_1) with an edge at 1.9

eV and a spectral shape similar to the $x=0.5$, and (2) a double-peak like structure (S_2). The step-like spectral feature has an additional offset representing dynamics that are uniform across the measured spectral range. In the $x=0.3$ sample, this offset is negative with decreasing amplitude at higher temperatures. This is consistent with a photoinduced increase in spectral weight at low energies, with a corresponding reduction in the narrow range of energies measured here. The shape of (S_1) is qualitatively similar to the change in reflectivity that occurs with the closing of the charge-ordering gap, as measured through the temperature and magnetic field dependence of the optical spectrum [14, 30].

The spectral dynamics observed for $x=0.3$ exhibit important similarities and differences with the $x=0.5$ data. The first spectral component S_1 (common to both $x=0.3$ and $x=0.5$) is characterized by dynamics with fast and slow components that are similar to those observed for $x=0.5$. The fast component, τ_1 , has been associated with thermalization of the initially excited carriers, and the slow component associated with meta-stable melting of the charge ordering [7, 31]. As shown in figure 5a, the spectrum S_1 is qualitatively similar to the change in spectrum due to a destruction of the charge ordering, either through the CMR effect or heating above the transition temperature [14, 30], and the dynamics T_1 therefore represent a partial loss of charge ordering due to photo-induced charge delocalization.

The second spectral component (S_2) is characterized by an intermediate time constant, τ_2 (~ 9 ps), which is similar to that observed in the AFM RXD data, but is not observed in the optical data at $x=0.5$ doping.

In this spectral region, the optical conductivity is dominated by charge-transfer and $d-d$ transitions, which can be modeled by a sum of oscillators [26]:

$$\epsilon(\omega) = 1 + 4\pi \sum_j \frac{f_j}{\omega_j^2 - \omega^2 - i\gamma_j\omega} \quad (2)$$

The oscillators are centered at $E_j = \hbar\omega_j$, with widths γ_j and oscillator strengths f_j . Figure 5b shows a fit to the spectrum S_2 , modeled as a change in oscillator strengths for oscillators at 1.64, 2.32, and 2.63 eV. The energies and widths of these peaks are consistent with previous models of the static reflectivity via $d-d$ and charge transfer transitions [26].

The origin of the spectral features are further elucidated by tracking the dynamics as a function of temperature as shown in figure 6. Detailed temperature dependent measurements of $\delta R/R$ at 1.37 eV and 2.07 eV clearly distinguish contributions to the different spectral components. The dynamics were characterized by an exponential fit with two time constants. For both $x=0.5$ and $x=0.3$ samples, the amplitude of the $\delta R/R$ signal increases sharply as the temperature is lowered below T_{CO} but shows no change at T_N (figure 6b, green diamonds, red triangles). For the $x=0.3$ doping, the time-constant for the intermediate component of the dynamics, (τ_2), is shown in figure 6(a), and varies continuously from 3 ps at $T_{F/A}$ to 14

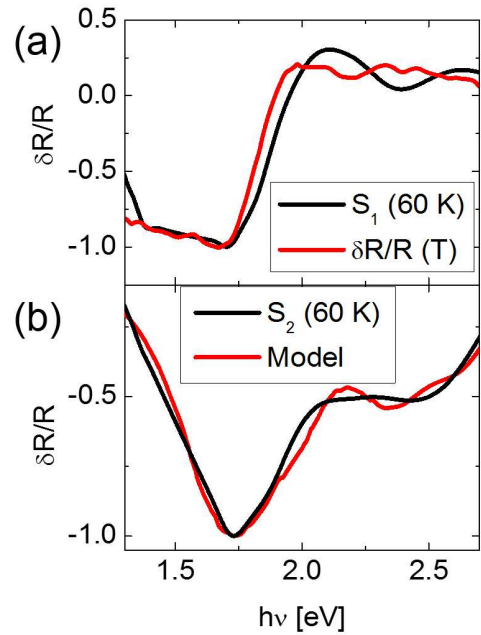


FIG. 5. (a) Comparison of dynamic spectral feature S_1 at 60 K and change in reflectivity across the charge/orbital ordering transition, given by $(R(T < T_{CO/OO}) - R(T > T_{CO/OO}))/R(T < T_{CO/OO})$ [14, 30] (b) Spectral feature S_1 and a fit from an oscillator model as described in the text.

ps at 20 K. The amplitude of this component increases below $T_{F/A}$ (figure 6(b)), increasing by a factor of 3 between $T_{F/A}$ and 20 K.

Note that in the reflectivity data, there is no evidence of the AFM transition at either doping, while there are strong transitions at both the ferromagnetic ($T_{F/A}$) and charge ordering (T_{CO}) transitions. The onset of the second spectral component at $T_{F/A}$, and the absence of this component in the $x=0.5$ data, indicates that the intermediate time scale is associated with the onset of phase separation at $T_{F/A}$ in the $x = 0.3$ doped sample.

For $x = 0.3$, the formation of the metastable photoexcited state is limited by the intermediate time-constant τ_2 that is observed in spectral component S_2 . While component S_1 is similar to the spectral shift observed in the CMR effect, and the temperature dependence suggests that this spectral feature is associated with a reduction of the charge-ordering, no photo-induced metallic state is observed in the $x=0.5$ doped sample. We therefore conclude that formation of the state of the $x=0.3$ sample on the time-scales for which a global photo-induced metallic state has been confirmed is limited by the S_2 component.

DISCUSSION

Through comparison with the optical data, we identify the processes behind both time-constants in the AFM scattering dynamics. After optical excitation, reflectivity spectra

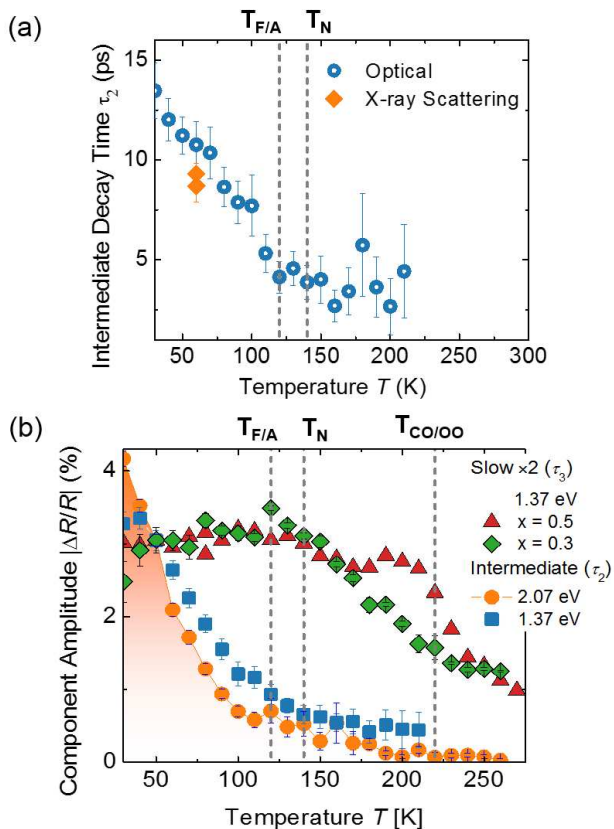


FIG. 6. Time constants and absolute values of the amplitudes for dR/R data probed at 1.37 and 2.07 eV in the $x=0.3$ sample, and at 1.37 in the $x=0.5$ sample. (a) Time-constant for intermediate component. The orange diamonds represent the time-constants for the AFM RXD data shown in figure 1. (b) Amplitudes of the intermediate time-scale (3-10 ps, shown in (a)) and slow ($\gg 60$ ps) components of the $\delta R/R$ signals.

show a prompt change associated with a destruction of the charge-ordered state. The 300 fs initial loss of x-ray diffraction strength in the AFM scattering intensity results from an incomplete destruction of the antiferromagnetism associated with this melting of the charge ordering.

At 1.5 eV, the initial excitation is thought to be a local Mn-O intrasite charge-transfer transition, and it has been suggested that Jahn-Teller distortions relax on ultrafast time-scales after this excitation [8, 13]. The formation of macroscopic conducting pathways indicates that this excitation eventually delocalizes. The invariance of the RXD correlation length, and therefore the constant characteristic AFM domain size, suggests that this occurs without the formation of large metallic domains. This is in contrast to what might be expected from spinodal decomposition of photo-excited metallic regions, where initial small local excitations subsequently cluster to form larger metallic regions [32].

Further loss of AFM scattering intensity occurs on the same 9 ps time-scale as the transient observed in optical reflectivity data, indicating that these dynamics are associated with the same process. The magnitude of the intermediate compo-

nent of dR/R increases sharply at $T_{F/A}$, and these time-scale dynamics occur only in the mixed phase. Moreover, static RXD data shows a strongly increasing scattering intensity below $T_{F/A}$. The scattering intensity depends on the cooperative interaction between AFM and FM order parameters [24], and optical excitation of either parameter will result in the loss of scattering intensity. The optical measurements are insensitive to the AFM phase, and we therefore attribute the 9 ps loss in AFM scattering intensity with a reduction of the FM order parameter, which appears in the AFM signal through this cooperative effect.

RXD data and previous measurements [9] show perturbation of both AFM and FM order parameters on 100 fs time-scales. The time-scale of the intermediate dynamics are consistent with coupling of the excitation to the lattice [33], where the transient suppression of the AFM ordering occurs. The presence of this time-scale in the optical data and in the RXD data, and the measured sensitivity of the time constant to the transition into the mixed phase, suggests that this time-constant represents a change in the global properties of the sample that affects both FM and AFM states. We propose that coupling between magnetic ordering and long-range lattice strains through compensation regions at the boundary between phases naturally explains the onset of dynamics in the AFM scattering associated with the mixed phase. Through a magnetic/lattice interaction, the reduction of magnetic ordering changes the shape of the unit cell and ultimately the strain in the compensation regions between different magnetic domains.

The time-scale and temperature dependence of this time constant is consistent with a strong electron-lattice coupling at high temperature and the development of an electron-lattice bottleneck below $T_{F/A}$. We attribute the temperature dependence of this time-constant (figure 6a) to Arrhenius-like behavior due to the formation of an energy barrier between the equilibrium insulating state and the quasi-equilibrium photo-excited metallic state. Below $T_{F/A}$, the photo-excitation establishes a new free energy minimum which is reached by crossing an activation barrier dependent on the FM order parameter. This process is illustrated in figure 7(a).

In this model, the excited configuration is treated as a thermodynamically equilibrated mix between local insulating and metallic states, with the transition from the purely insulating state dependent on the thermal energy of the system. In the Arrhenius model, the reaction rate follows the relation

$$r = 1/\tau = r_0 e^{-E_A/kT} \quad (3)$$

Both the activation energy (E_A), and the pre-exponential coefficient (r_0), can in principle be temperature dependent, however the dominant temperature dependence is a slowing of the rate at low temperature due to the exponential term. For a constant r_0 , the measured time-constants would imply a photo-induced local minima below $T_{F/A}$, with an activation energy that decreases but remains non-zero as the tem-

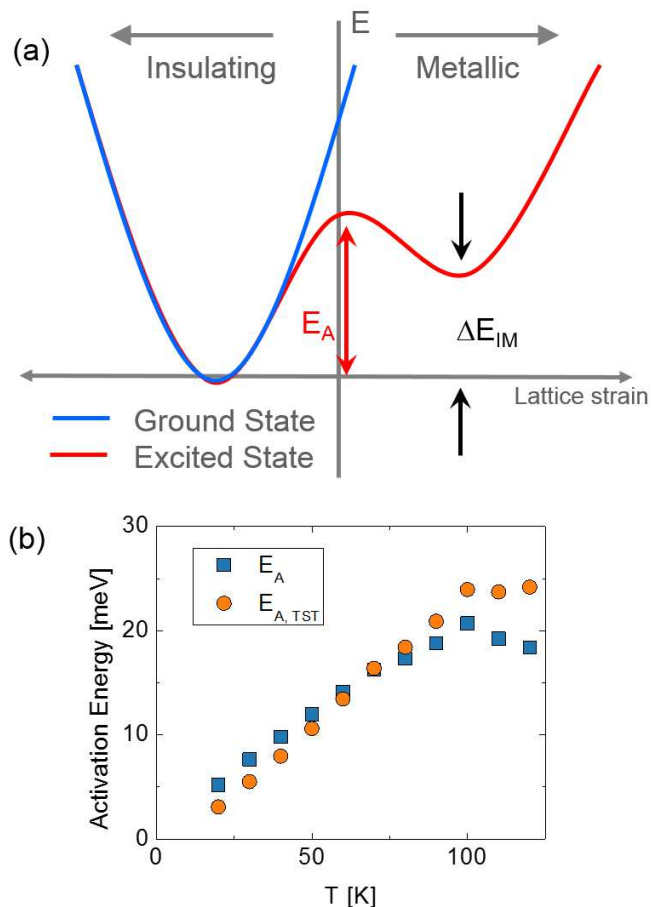


FIG. 7. (a) Energy diagram of equilibrium (blue) and photoexcited (red) states. Inset equations show the thermal equilibrium population ratio of metallic and insulating states and time constant for conversion from metallic to insulating. (b) Calculated activation energies, with different temperature dependences of the leading tau term in the arrhenius equation, derived from the measured intermediate time constant. There is no gap above $T_{F/A}$, so the activation is zero above this temperature. (b) Activation energy with $r_0 = 0.7$ ps (E_A , squares) and with $r_0 = kT/h$ from transition state theory ($E_{A,TST}$, circles).

perature is lowered, as shown in figure 7(b). Transition state theory approximates the temperature dependence of the pre-exponential coefficient as $r_0 = kT/h$, where h is Plancks constant [34]. The resulting activation energy is qualitatively similar to the case of constant r_0 , but extrapolating to less than zero values at low temperature.

At $T_{F/A}$, the introduction of FM domains into the AFM background leads to structural inhomogeneities, and it has been shown recently that structural grain boundaries can have profound effects on magnetic domains in manganites[18–23]. We propose a similar mechanism, with interactions between the FM and AFM phases through frozen-in structural inhomogeneities that are responsible for the observed coupled dynamics. The intermediate time-constant appears in specific spectral features centered at 1.75 eV and 2.5 eV, at energies where onsite charge-transfer excitations contribute to the op-

tical constants[26]. A change in the charge-transfer optical transition matrix, due to a change in the lattice structure, is consistent with these spectral features.

Below $T_{F/A}$, the grain boundaries of the AFM phase are frozen in and remain so even after photo-induced conversion to the metallic state. The lack of dynamics in the scattering correlation length throughout the excitation and recovery process indicates a systematic memory of the FM/AFM boundaries, and the metallic phase develops from the composite FM/AFM insulating phase without disturbing these boundaries. Inhomogeneous strain regions remain fixed throughout photo-induced phase transition, resulting in a relatively short-lived metallic phase. In contrast, re-ordering of these boundaries through forced magnetic alignment in the magnetic-field induced CMR transition would result in a phase that is stable until the compensation regions are removed fully through heating of the sample.

SUMMARY

In summary, common features in the dynamics of x-ray scattering measurements and transient optical spectra provide new insights into the physics underlying the photo-induced metallic phase in PCMO. X-rays directly probe the dynamics of the AFM ordering, while optical spectra relate to onsite charge transfers and CO. Taken together, these results characterize the changes in the coexisting FM and AFM phases that result in the formation of the meta-stable photo-induced phase. These results suggest that while the metallic phase may be reached immediately through optical excitation of the charge ordering, the meta-stable metallic phase is reached only after 15 ps at low temperatures. This indicates previously observed interactions between the phase-separated FM and AFM states play a crucial role in the formation of the photo-induced metallic state, with the temperature-dependence of the intermediate time constant consistent with a first-order phase transition across an activation barrier related to the FM order parameter.

This material is based upon work supported by the U.S. Department of Energy, Office of Science, Office of Basic Energy Sciences (BES) under Contracts No. DEAC02-05CH11231 (LBNL) and No. DE-AC02-76SF00515 (SLAC). This research used resources of the Advanced Light Source (LBNL) and the Linac Coherent Light Source (SLAC) which are DOE Office of Science User Facilities. S.Z., Y.Z., G.C., and R.A.K., acknowledge support from the BES Materials Sciences and Engineering Division through the Ultrafast Materials Program at LBNL. M.C.L. and R.W.S. acknowledge support from Laboratory Directed Research and Development (LDRD) funding from LBNL provided by the Director, Office of Science, of the U.S. Department of Energy.

-
- [1] Y. Tokura, Rep. Prog. Phys. **69**, 797 (2006).
- [2] Y. Tokura, Y. Tomioka, H. Kuwahara, A. Asamitsu, Y. Moritomo, and M. Kasai, J. Appl. Phys. **79**, 5288 (1996).
- [3] P. Lee, N. Nagaosa, and X.-G. Wen, Reviews of Modern Physics **76**, 17 (2006).
- [4] E. Dagotto, T. Hotta, and A. Moreo, Physics Reports **344**, 1 (2001).
- [5] Y. Tomioka, A. Asamitsu, H. Kuwahara, Y. Moritomo, and Y. Tokura, Phys. Rev. B **53**, R1689 (1996).
- [6] K. Miyano, T. Tanaka, Y. Tomioka, and Y. Tokura, Phys. Rev. Lett. **78**, 4257 (1997).
- [7] M. Rini, R. Tobey, N. Dean, S. Wall, H. Ehrke, Y. Tomioka, Y. Tokura, R. Schoenlein, and A. Cavalleri, Journal of Physics: Conference Series **148**, 012013 (2009).
- [8] P. Beaud, C. A., S. Mariager, L. Rettig, G. Ingold, C. Dornes, S.-W. Huang, A. Johnson, R. M., T. Huber, T. Kubacka, A. Ferrer, H. Lemke, C. M., D. Zhu, J. Glowina, M. Sikorski, A. Robert, H. Wadati, N. M., M. Kawasaki, Y. Tokura, S. Johnson, and U. Staub, Nature Materials **13**, 923 (2014).
- [9] T. Li, A. Petz, L. Mouchliadis, J. Yan, T. A. Lograsso, I. E. Perakis, and J. Wang, Nature **496**, 69 (2013).
- [10] M. Rini, Y. Zhu, S. Wall, R. I. Tobey, H. Ehrke, T. Garl, J. W. Freeland, Y. Tomioka, Y. Tokura, A. Cavalleri, and R. W. Schoenlein, Phys. Rev. B **80**, 155113 (2009).
- [11] M. Rini, R. Tobey, N. Dean, J. Itatani, Y. Tomioka, Y. Tokura, R. W. Schoenlein, and A. Cavalleri, Nature **449**, 72 (2007).
- [12] D. Polli, M. Rini, S. Wall, R. Schoenlein, Y. Tomioka, Y. Tokura, G. Cerullo, and A. Cavalleri, Nature Materials **6**, 643 (2007).
- [13] J. H. Jung, K. H. Kim, T. W. Noh, E. J. Choi, and J. Yu, Phys. Rev. B **57**, R11043 (1998).
- [14] Y. Okimoto, Y. Tomioka, Y. Onose, Y. Otsuka, and Y. Tokura, Phys. Rev. B **59**, 7401 (1999).
- [15] H. Lee, J. Jung, K. Kim, M. Kim, T. Noh, Y. Moritomo, Y. Wang, and X. Wei, Physica C **364-365**, 614 (2001).
- [16] M. Fiebig, K. Miyano, Y. Tomioka, and Y. Tokura, Applied Physics Letters **74**, 2310 (1999).
- [17] M. Fiebig, N. P. Duong, T. Satoh, B. B. V. Aken, K. Miyano, Y. Tomioka, and Y. Tokura, J. Phys. D: Appl. Phys. **41**, 164005 (2008).
- [18] D. Saurel, C. Simon, A. Brûlet, A. Heinemann, and C. Martin, Phys. Rev. B **75**, 184442 (2007).
- [19] D. Saurel, C. Simon, A. Pautrat, C. Martin, C. Dewhurst, and A. Brûlet, Phys. Rev. B **82**, 054427 (2010).
- [20] P. G. Radaelli, R. M. Ibberson, D. N. Argyriou, H. Casalta, K. H. Andersen, S.-W. Cheong, and J. F. Mitchell, Phys. Rev. B **63**, 172419 (2001).
- [21] M. H. Burkhardt, M. A. Hossain, S. Sarkar, Y.-D. Chuang, A. G. Cruz Gonzalez, A. Doran, A. Scholl, A. T. Young, N. Tahir, Y. J. Choi, S.-W. Cheong, H. A. Dürr, and J. Stöhr, Phys. Rev. Lett. **108**, 237202 (2012).
- [22] K. Ahn, T. Lookman, and B. A.R., Nature **428**, 401 (2004).
- [23] J. Turner, K. Thomas, J. P. Hill, M. A. Pfeifer, K. Chesnel, Y. Tomioka, Y. Tokura, and S. Kevan, New Journal of Physics **10**, 053023 (2008).
- [24] S. Y. Zhou, Y. Zhu, M. C. Langner, Y.-D. Chuang, P. Yu, W. L. Yang, A. G. Cruz Gonzalez, N. Tahir, M. Rini, Y.-H. Chu, R. Ramesh, D.-H. Lee, Y. Tomioka, Y. Tokura, Z. Hussain, and R. W. Schoenlein, Phys. Rev. Lett. **106**, 186404 (2011).
- [25] G. L. Dakovski, P. Heimann, M. Holmes, O. Krupin, M. P. Minitti, A. Mitra, S. Moeller, M. Rowen, W. F. Schlotter, and J. J. Turner, J. Synchrotron Rad. **22**, 152021 (2015).
- [26] A. S. Moskvina, A. A. Makhnev, L. V. Nomerovannaya, N. N. Loshkareva, and A. M. Balbashov, Phys. Rev. B **82**, 035106 (2010).
- [27] R. A. Kaindl, M. Woerner, T. Elsaesser, D. Smith, J. Ryan, G. Farnan, M. McCurry, and D. G. Walmsley, Science **287**, 470 (2000).
- [28] G. Coslovich, C. Giannetti, F. Cilento, S. Dal Conte, T. Abebaw, D. Bossini, G. Ferrini, H. Eisaki, M. Greven, A. Damascelli, and F. Parmigiani, Phys. Rev. Lett. **110**, 107003 (2013).
- [29] A. Pogrebna, N. Vujičić, T. Mertelj, T. Borzda, G. Cao, Z. A. Xu, J.-H. Chu, I. R. Fisher, and D. Mihailovic, Phys. Rev. B **89**, 165131 (2014).
- [30] Y. S. Lee, T. Arima, S. Onoda, Y. Okimoto, Y. Tokunaga, R. Mathieu, X. Z. Yu, J. P. He, Y. Kaneko, Y. Matsui, N. Nagaosa, and Y. Tokura, Phys. Rev. B **75**, 144407 (2007).
- [31] R. Averitt and A. Taylor, Journal of Physics: Condensed Matter **14**, R1357R1390 (2002).
- [32] J. Cahn, Journal of Chemical Physics **42**, 93 (1965).
- [33] A. Kirilyuk, A. V. Kimel, and T. Rasing, Rev. Mod. Phys. **82**, 2731 (2010).
- [34] D. Truhlar, B. Garrett, and S. Klippenstein, J. Phys. Chem. **100**, 12771 (1996).